ACS Photonics

pubs.acs.org/journal/apchd5

Article

On-Chip Fabry–Perot Bragg Grating Cavity Enhanced Four-Wave Mixing

Shengjie Xie,[§] Yang Zhang,[§] Yiwen Hu, Sylvain Veilleux, and Mario Dagenais*

Cite This: *ACS Photonics* 2020, 7, 1009–1015

Read Online

ACCESS | Metrics & More | Article Recommendations | Supporting Information

ABSTRACT: Optical microcavity based four-wave mixing (FWM) and its various applications, such as entangled photon pair generation, have been intensively studied in the past few years. Compared to the microring cavities that most researchers have been focusing on, here, we report the generation of FWM photons with Fabry–Perot Bragg grating cavities (FPBG) using the Si_3N_4/SiO_2 platform. By leveraging the large, nonuniform and symmetrical dispersion and tunability of our grating cavity, a unique strategy is established to compensate the strong normal dispersion of the waveguide and phase matching condition is achieved on a thin Si_3N_4 film, which is critical for efficient wavelength conversion. We develop an analytical model to optimize the nonlinear conversion efficiency of FWM, and we also introduce tapered grating in the FPBG to reduce the grating loss from 3.5 dB/cm to 0.36 dB/cm. With a 5.3 dBm pump power, the nonlinear conversion efficiency is characterized to be −37.7 dB. Our work demonstrates that FPBG is a promising on-chip platform for entangled photon pair generation and quantum communication applications.

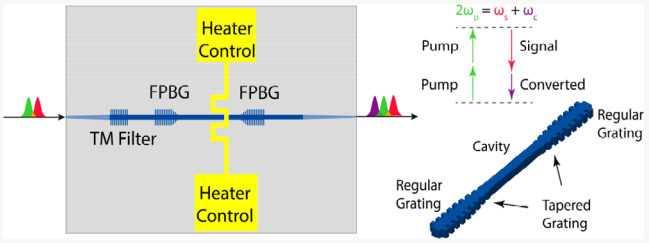

KEYWORDS: *Fabry–Perot cavity, nonlinear optics, Kerr effect, microresonator, dispersion compensation*

In the past decade, four-wave mixing (FWM), a third-order optical nonlinear process, has become an area of increasing interest. FWM optical devices have many applications in all-optical signal processing such as high-speed sampling, switching, wavelength conversion, amplification, and comb generation.[1−4]

For integrated implementation of FWM, silicon (Si) has been widely considered due to its CMOS compatibility, high third-order nonlinearity, and high index contrast.[5,6] However, the nonlinear losses originating from two-photon absorption (TPA) and free carrier absorption at telecom wavelengths limit the maximum power that can be sent into Si. More recently, a great amount of research interests has focused on exploring other nonlinear materials as an alternative to Si such as silicon nitride (Si_3N_4)[7], AlGaAs,[8] and lithium niobate.[9−11] Si_3N_4 stands out as a promising candidate due to its ultralow loss[7] and its CMOS compatibility, which makes the mass production of optical circuits possible and might appreciably reduce processing costs.

The FWM effect can be dramatically enhanced when using a high-Q optical resonator thanks to the strong enhancement of the intracavity electric field. Most efforts for on-chip applications have been put on ring-like resonators because of their ultralow-loss and fabrication simplicity. Many accomplishments have been realized in ring resonator based FWM processes, from wavelength conversion and photon pair generation[12−14] to optical comb and soliton generation.[7,11,15−18] In this work, however, we will focus on a Fabry–Perot Bragg grating cavity enhanced FWM process. Unlike ring resonators, which will generate FWM signals over a large bandwidth, the Fabry–Perot Bragg grating cavity enhanced FWM (FPBG-FWM) process will only generate FWM signals within the photonic stopband. By carefully designing the grating cavity parameters, we can generate FWM signals at desired wavelengths, which could enable many applications in entangled photon pair generation and quantum communication. Few publications have focused on the FPBG-FWM process,[19−21] and just recently, it has been implemented on an integrated platform.[21]

In this paper, we study the FPBG-FWM on a Si_3N_4/SiO_2 platform, from analytical derivations to experimental demonstrations. A numerical model based on the transfer matrix of Bragg grating is developed to optimize the structural design of FPBG-FWM device. We achieve a conversion efficiency of −37.7 dB with a low on-chip pump power of 5.3 dBm. A unique loss reduction strategy is proposed and experimentally demonstrated in this paper, which is critical for an efficient FWM process. We further demonstrate that, unlike Si_3N_4 ring resonators, by leveraging the large, nonuniform and symmetrical dispersion induced by the grating, phase matching

Received: December 2, 2019
Published: March 13, 2020

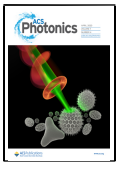

https://dx.doi.org/10.1021/acsphotonics.9b01697
ACS Photonics 2020, 7, 1009–1015

condition is controllably achievable on thin Si_3N_4 film without having to adjust the waveguide geometry and implement dispersion engineering, which lifts a significant fabrication constrain and makes the efficient FWM process more accessible.

THEORY OF FPBG-FWM

To build the theoretical model of FPBG-FWM, we first consider a waveguide that has a length of L. Under a small-signal approximation, the field amplitudes of the pump wave E_p, the signal wave E_s, and the converted FWM wave E_c satisfy the following nonlinear propagation equations:[22,23]

$$\frac{\partial E_p}{\partial z} = -\frac{\alpha_p}{2}E_p \tag{1}$$

$$\frac{\partial E_s}{\partial z} = -\frac{\alpha_s}{2}E_s \tag{2}$$

$$\frac{\partial E_c}{\partial z} = -\frac{\alpha_c}{2}E_c + i\gamma {E_p}^2 {E_s}^* e^{i\Delta k z} \tag{3}$$

where $\Delta k = 2k_p - k_s - k_c$, with k_p, k_s, k_c the propagation constants of the pump, the signal, and the converted wave, respectively. The nonlinear coefficient γ is related to the Kerr coefficient n_2, the effective mode size A_{eff}, and the converted frequency ω_c by $\gamma = n_2\,\omega_c/cA_{eff}$. For a relatively small pump-signal frequency detuning, as in our case, we can assume a constant propagation loss coefficient, that is, $\alpha \approx \alpha_p \approx \alpha_s \approx \alpha_c$. By applying the boundary conditions $E_p\ (z = 0) = E_{p0}$, $E_s\ (z = 0) = E_{s0}$, $E_c\ (z = 0) = 0$, we get $\eta = \frac{P_c^{out}}{P_s^{in}} = |\gamma P_p L'|^2$, where $L'^2 = L^2 e^{-\alpha L}\left|\frac{1-\exp(-\alpha L + i\Delta k L)}{\alpha L - i\Delta k L}\right|^2$

Figure 1a illustrates the electric fields in a Fabry–Perot resonator when an electric field $E^{(in)}$ is incident upon mirror 1. Inside the cavity, there are the forward-traveling wave and the backward-traveling wave, which can be represented as follows:

$$\text{at } z = 0,\ E^{(forward)} = t_1 E^{(in)} + r_1 e^{-\alpha L/2 - ikL} E^{(backward)} \tag{4}$$

$$\text{at } z = L,\ E^{(backward)} = r_2 e^{-\alpha L/2 - ikL} E^{(forward)} \tag{5}$$

where r_1 and r_2 are the electric-field mirror reflectivities, and t_1 and t_2 are the electric-field mirror transmittivities. They satisfy $|r|^2 + |t|^2 \approx 1$, neglecting the minor propagation loss from the mirrors. By solving the above equation, we get an expression for the intensity enhancement (IE) given by

$$IE = \left|\frac{E^{(forward)}}{E^{(in)}}\right|^2 + \left|\frac{E^{(backward)}}{E^{(in)}}\right|^2 = \left|\frac{t_1}{1 - r_1 r_2 \exp(-\alpha L - i2k_i L)}\right|^2 (1 + |r_2 e^{-\alpha L/2}|^2) \tag{6}$$

where i can be substituted by p, s, and c. The field enhancement is maximized at the cavity resonant frequencies. Therefore, the small-signal FWM conversion efficiency enhanced by a Fabry–Perot cavity is finally given by

$$\eta = |\gamma P_p L'|^2 (IE_p)^2 (IE_s)(IE_c) \tag{7}$$

It contains the physics of both FWM and the resonator enhancement. The first factor, $|\gamma P_p L'|^2$, is the FWM conversion efficiency in a straight waveguide with an effective length of L'.

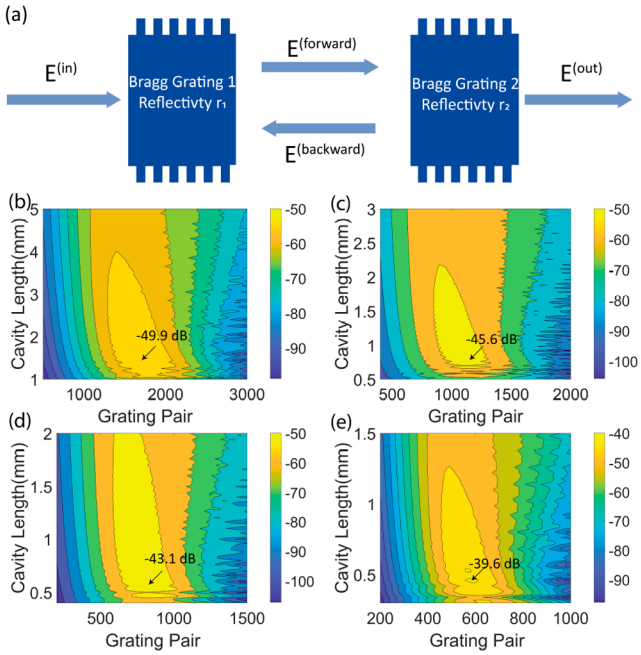

Figure 1. (a) Illustration of the Fabry–Perot cavity under study. (b–e) Simulation of the relationship between the FWM efficiency and the grating coupling strength by fixing other parameters, color bar representing the conversion dispersion in dB scale. (b) Taking the coupling strength to be $\kappa = 54$ cm^{-1}, the maximum efficiency is $n = -49.9$ dB in simulation; (c) for a coupling strength $\kappa = 94$ cm^{-1}, the maximum efficiency $n = -45.6$ dB; (d) for a coupling strength $\kappa = 133$ cm^{-1}, the maximum efficiency $n = -43.1$ dB; (e) for a coupling strength $\kappa = 193$ cm^{-1}, the maximum efficiency $n = -39.6$ dB.

The effective length L' contains both the phase mismatch and the propagation loss. The last three factors, $(IE_p)^2$ $(IE_s)(IE_c)$ give the intensity enhancement inside the cavity for the pump, the signal, and the converted wave, respectively. The enhancement comes from both light recirculation and the energy buildup. As indicated above, the nonlinear coefficient γ is related to the Kerr coefficient n_2, the effective mode size A_{eff}, and the converted frequency ω_c. Since the Kerr coefficient of Si_3N_4 is 10-times larger than that of SiO_2, a better mode confinement will provide a larger nonlinear coefficient. In this paper, we work with 300 nm thick low-pressure chemical vapor deposited (LPCVD) Si_3N_4, which provides a good mode confinement and is free from excessive film stress.

BRAGG GRATING DESIGN AND LOSSES REDUCTION

From eq 6, it is obvious that the larger the reflectivity r and the lower the loss α, the higher the IE on resonance. Thus, to achieve high FWM efficiency, a Bragg grating with strong coupling strength and low loss is highly desirable. Here, the transfer matrix method, developed in our previous work,[24] is the perfect tool to implement the theoretical analysis of the FWM efficiency for a given Bragg grating geometry. From eq 6, the only unknown parameters for the IE factor are the mirrors reflectivity and transmittivity. We use the transfer matrix to calculate the r and t and to simulate the IE factor. In this way, we obtain the FWM efficiency. As shown in Figure 1b–e, as a demonstration, by fixing the grating loss to be 0.4 dB/cm, the cavity loss to be 0.3 dB/cm, the input pump power to be 0 dBm, the nonlinear coefficient to be 1.6 m^{-1} W^{-1}, and by increasing the grating coupling strength from 54 to 193 cm^{-1},

https://dx.doi.org/10.1021/acsphotonics.9b01697
ACS Photonics 2020, 7, 1009–1015

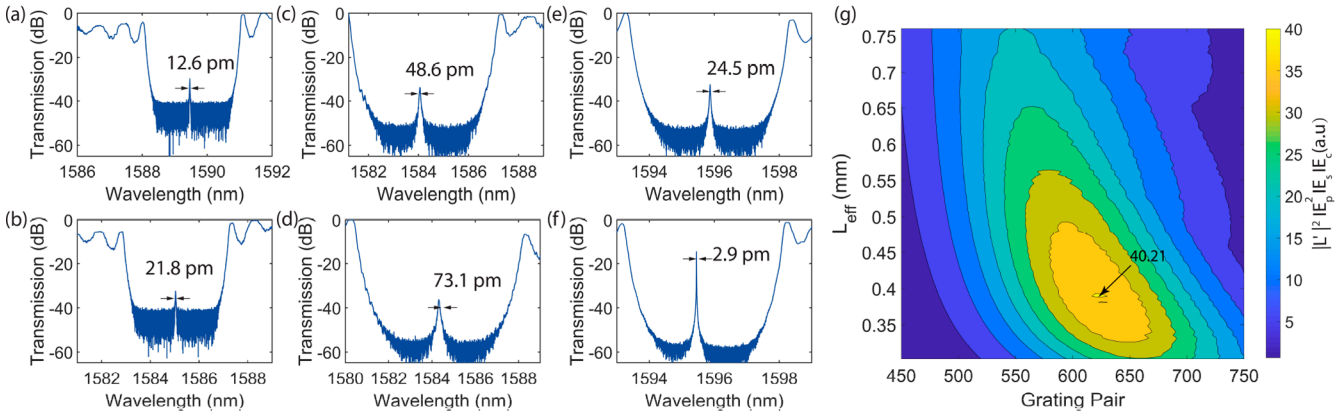

Figure 2. Experimental characterization of the grating loss for different grating coupling strength. (a) κ = 77 cm^{-1}, measured grating loss 1.95 dB/cm. (b) κ = 110 cm^{-1}, measured grating loss 3.1 dB/cm. (c) κ = 155 cm^{-1}, measured grating loss 6.6 dB/cm. (d) κ = 201 cm^{-1}, measured grating loss 12.0 dB/cm. (e) Transmission pattern of a normal PSBG with a coupling strength of 125 cm^{-1}. (f) Transmission pattern of PSBG with tapered grating with a coupling strength of 125 cm^{-1}. (g) Simulation of the enhanced factor $|L'|^2$ $(IE_p)^2(IE_s)(IE_c)$ with a grating loss of 0.36 dB/cm and a cavity loss of 0.33 dB/cm. The enhanced factor reaches the peak, 40.21, with 625 grating pairs for each mirror and 390 μm effective cavity length.

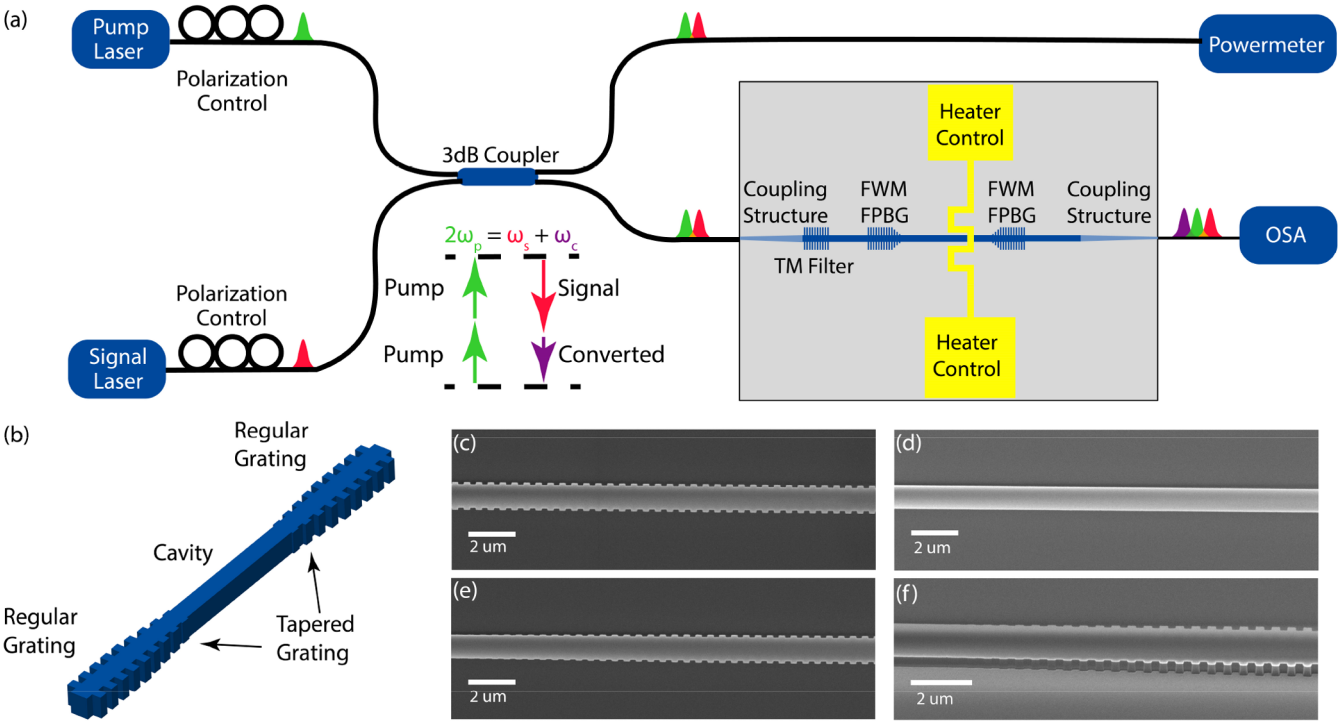

Figure 3. (a) Schematic of the experimental setup. An integrated heater is added on top of the cavity center. (b) Schematic of the FPBG, when tapered gratings are added between the regular grating and the cavity to facilitate mode conversion between the cavity mode and the grating Bloch mode. (c–f) SEM images at different locations along a fabricated FPBG. (c) Top view of the periodic Bragg grating. (d) Top view of the straight waveguide in the cavity center. (e) Top view of the linearly tapered grating connecting a regular Bragg grating and the cavity. (f) Tilted view of the linearly tapered Bragg grating.

the simulated FWM conversion efficiency η is improved by more than 10 dB. Next, the transfer matrix method is also used to extract the small losses, $\alpha_{grating}$ and α_{cavity}, for the given Bragg grating geometry.[24] To characterize the grating loss of a given grating geometry, we design a set of π phase-shifted Bragg grating (PSBG) with different coupling strengths. The quality factor of the PSBG resonant peak is directly related to the grating loss. As shown in Figure 2a–d, when the grating coupling strength increases from 77 cm^{-1} to 201 cm^{-1}, the measured 3-dB linewidth of the resonant peak increases from 12.6 to 73.1 pm, corresponding to a grating loss increases from 1.95 dB/cm to 12 dB/cm. This is not desirable since significantly higher grating loss will deal excessive penalties for the FWM efficiency. The total FWM efficiency will not benefit from strongly coupled grating without addressing its excessive grating losses. In fact, like 1-D photonic crystal, the large grating loss of the strongly coupled grating mainly comes from the mode mismatch between the waveguide mode and the grating Bloch mode.[25−27] Whenever the light travels through the interface between the Bragg grating and the cavity, it will experience such a mode mismatch loss. For a FPBG cavity, the light will travel multiple times across the interface of the waveguide and the grating, and the mode mismatch can be substantial. Thus, an adiabatic tapered grating is added

https://dx.doi.org/10.1021/acsphotonics.9b01697
ACS Photonics 2020, 7, 1009−1015

between the Bragg grating and the cavity, which facilitates the adiabatic mode conversion between a cavity mode and a grating Bloch mode, and significantly reduces the grating loss. Figure 2e and f show that, by introducing a tapered grating (as shown in Figure 3b), which linearly reduces the grating width variation, the measured 3-dB linewidth of the resonant peak is reduced from 24.5 to 2.9 pm, corresponding to a grating loss reduction from 3.5 dB/cm to 0.36 dB/cm, which is comparable to the grating loss of weakly coupled Bragg grating.

FWM EXPERIMENTAL RESULTS AND ANALYSIS

Experimentally, the Bragg grating has a coupling strength of 193 cm^{-1}. The grating is defined by a sidewall corrugation, and the width variation is from 1.0 to 1.2 μm. The cavity geometry is designed as 1.0 μm × 0.3 μm. The Bragg grating and the cavity geometry guarantee that only the fundamental mode is excited on chip so that no multimode noise will be observed in the transmission signal. The nonlinear coefficient γ can be calculated by

$$\gamma = \sqrt{\left(\frac{n_2^{SiN}\omega}{cA_{SiN}}\right)^2 F^3 + \left(\frac{n_2^{SiO2}\omega}{cA_{SiO2}}\right)^2 (1-F)^3} \quad (8)$$

where n_2^{SiN} represents the Si_3N_4 nonlinear coefficient, n_2^{SiO2} represents the SiO_2 nonlinear coefficient, A_{SiN} and A_{SiO2} represent the effective mode area in Si_3N_4 and SiO_2, respectively, and F represents the power fill factor, namely the fraction of power that is confined in the Si_3N_4 core region. The nonlinear coefficient γ of our current design is calculated to be 0.99 m^{-1} W^{-1}. Following the transfer matrix method, we extract a grating loss of 0.36 dB/cm and a cavity loss of 0.33 dB/cm for a tapered PSBG and a FPBG, respectively. On the basis of all the losses and grating coupling strength information, we optimize our FWM Bragg grating with eq 6. It is worth noting that, in eq 6, since the nonlinear coefficient γ and the pump power P can be viewed as preset parameters if the waveguide geometry and input power are fixed, only the enhanced factor $|L'|^2 (IE_p)^2(IE_s)(IE_c)$ will be optimized by engineering the grating and the cavity design. As shown in Figure 2g, the optimized FWM cavity design is found to be 625 periods of Bragg grating, including 20 periods of linearly tapered grating, for each mirror and an effective cavity length of 390 μm. The maximum enhanced factor from the cavity is 40.21. The dimension of the FPBG is comparable to a typical Si_3N_4 ring resonator.

The experiment schematic is shown in Figure 3a. We use two tunable continuous wave (CW) lasers as the pump beam and signal beam, respectively, whose polarizations are controlled independently. After the polarization controllers (PCs), the polarization states of both beams are aligned to be TE polarized. The wavelengths of both waves are tuned so that each matches one of the resonant peaks. The beams are combined by a 3 dB coupler, and then half of the combined beam is monitored by a powermeter while the other half is coupled on chip using a fiber-chip butt coupling approach. A 3.0 dB coupling loss is achieved with a coupling structure designed to facilitate efficient fiber-chip butt coupling.[28] The output light is analyzed by an optical spectrum analyzer (OSA). Our fabrication starts from a Si substrate with 10 μm thermal SiO_2. A 300 nm LPCVD Si_3N_4 is deposited on the substrate. The chip is patterned by e-beam lithography (EBL) with ZEP-520A, a positive tone resist. After development, 20 nm chromium mask is deposited using a lift-off approach, which works as a dry etch hard mask followed by an induced coupled plasma (ICP) etching. After chromium removal, the sample is deposited with 4 μm plasma-enhanced chemical vapor deposition (PECVD) SiO_2 as a top cladding layer. As shown in Figure 3c–f, the regular Bragg grating, tapered Bragg grating, and the cavity are patterned by EBL with smooth boundaries. A smooth sidewall is achieved with ICP dry etching. Since the polarization-maintaining (PM) fiber we use can only ensure a 20–25 dB polarization extinction ratio, there is still some TM polarized light injected on chip. Because of the different effective index of the TE and TM mode, the central wavelengths of the TE stopband and TM stopband of the designed Bragg grating geometry are separated by 30–40 nm. Thus, the TM mode will not be rejected in the TE stopband. That is an important noise source and must be removed; otherwise, it will cover the weak FWM signal and make the FWM measurement impossible. Here we add an additional integrated Bragg grating whose TM stopband aligns with the TE stopband of the FWM Bragg grating to remove the residual on-chip TM noise. As shown in Figure 4a, without

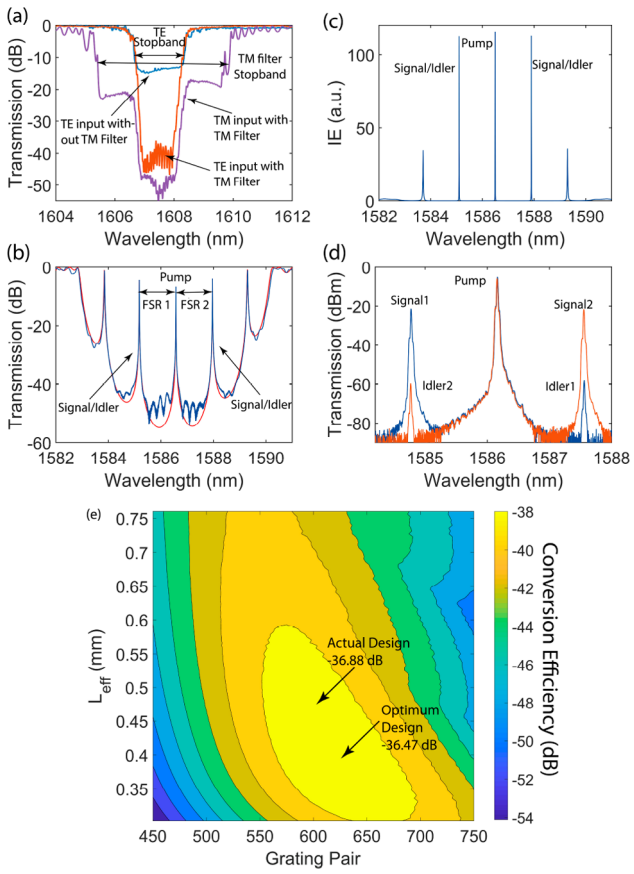

Figure 4. (a) Transmission of TE Bragg grating without TM noise filter and transmission pattern of TE Bragg grating with TM noise filter. The TE and TM stopbands overlap so that the TM noise inside the TE stopband is suppressed by around 30 dB. (b) Transmission of the FWM Bragg grating. The 3-dB linewidth of the resonant peak is measured to be 3.3 pm, corresponding to a quality factor of 480k. (c) Calculated *IE* factor inside the stopband. (d) Measured FWM signals. A −37.7 dB conversion efficiency is experimentally observed. (e) Simulation of the FWM conversion efficiency. The theoretical conversion efficiency of the actual device is slightly less than that of the optimum design due to fabrication uncertainty.

https://dx.doi.org/10.1021/acsphotonics.9b01697
ACS Photonics 2020, 7, 1009–1015

the TM filter, the TE stopband depth is limited to less than 20 dB by the TM noise. After adding an integrated TM filter and carefully aligning its stopband with the existing TE Bragg grating's stopband, the TE stopband depth is improved to better than 40 dB, which is favorable for FWM measurements. It is worth noting that, since the TM filter is essentially another Bragg grating and its loss is comparable to the grating loss of the grating loss of the FPBG, the insertion loss of the TM filter is negligible.

The experimental FWM measurement results are shown in Figure 4b–d. With the FWM Bragg grating, we observe five resonant peaks inside the stopband with the narrowest peak having a 3-dB linewidth of 3.3 pm (388 MHz). This corresponds to a quality factor of 480k. The pump and signal wavelengths are offset by one free spectral range (FSR) near 1586.5 nm. As shown in Figure 4c, the resonance enables more than 100-times intensity enhancement on all three resonant wavelengths. The FSR of the resonant peaks is measured to be around 1.39 nm (165.97 GHz). A 29 MHz FSR detuning, defined as $FSR_1 - FSR_2$, is measured as shown in Figure 4b and is much smaller when compared with the resonance line width.

With an on-chip incident pump power of 5.3 dBm and a signal power of −11.9 dBm, we observed an FWM conversion efficiency of −37.7 dB. As shown in Figure 4e, the calculated FWM efficiency of the optimum design should be −36.47 dB from eq 7. The actual fabricated device slightly deviates from the optimum design due to fabrication uncertainty. For the estimated experimental parameters, the maximum theoretical efficiency is calculated to be −36.88 dB, which is in reasonable agreement with the experimentally measured efficiency of −37.7 dB and thus supports the validity of our theory. It also shows that the design of FPBG has high tolerance to the fabrication uncertainties.

Dispersion is a critical factor in FWM since the FWM process is optimum when energy conservation and momentum conservation are both satisfied. A mismatch between the converted frequency and the resonant frequency of the cavity will limit the FWM efficiency. In most ring resonator based nonlinear applications, a zero or anomalous dispersion within a certain frequency range is favorable and is usually realized by carefully designing a thick Si_3N_4 core, typically more than 600 nm. Such thick LPCVD Si_3N_4 requires additional stress release process including annealing, multilayer deposition,[29,30] or the use of a photonic damascene process.[31] These methods increase the fabrication complexity, and some are not compatible with a CMOS process. However, in a FPBG-FWM platform, the grating induced dispersion can be a powerful tool to counteract the waveguide induced dispersion without requiring thick Si_3N_4 deposition and dispersion engineering. As shown in Figure 5a and b, the grating induced dispersion is not only way larger than the waveguide dispersion, which is around −1400 ps/(nm km), but also nonuniform and symmetrical with respect to the stopband center. An extremely strong, nonuniform and symmetrical grating dispersion indicates that, even if a conventional dispersion engineering approach is implemented, the resonances of the FPBG cavity will still not be equally distant unless the resonances, whose positions are determined by the combination of grating phase and cavity phase, are symmetrical within the stopband. While the grating dispersion is an additional dispersion mechanism compared with a ring resonator, it provides a new tool to offset the waveguide

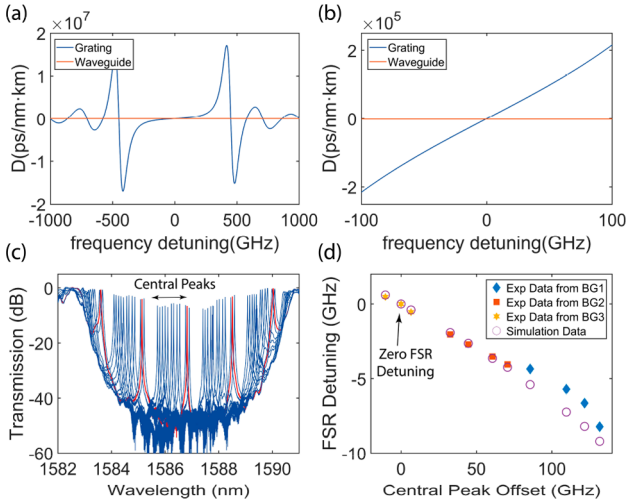

Figure 5. (a) Comparison of grating induced dispersion and waveguide induced dispersion. The grating dispersion is dominant compared to the waveguide dispersion. (b) Zoom-in dispersion comparison shows that the grating dispersion is still dominant around the stopband center. (c) Experimental results of thermal-tuning based dispersion engineering. Resonant peaks drift inside the stopband while leaving the stopband position unchanged. The red line represents the −5.6 MHz FSR detuning position. (d) FSR detuning changes with the central peak frequency offset showing that thermal tuning can effectively implement dispersion compensation. Experimental results are in good agreement with the transfer matrix simulation results. The simulation results indicate that zero FSR detuning is achievable.

dispersion without having to adjust the waveguide geometry. One can always locate three resonances where the grating dispersion can fully compensate the waveguide dispersion such that the phase matching condition is satisfied and the FWM efficiency is maximized. Taking waveguide dispersion into account, such three equal distant resonances are quasi-symmetrical with respect to the stopband center. Such mechanism does not rely on the waveguide geometry and can be adjusted with careful tuning of the cavity phase. The FSR of the resonances in a FPBG cavity is determined by

$$\phi_m + \frac{2\pi n L \nu_m}{c} = m\pi \tag{9}$$

$$\phi_{m+1} + \frac{2\pi n L \nu_{m+1}}{c} = (m+1)\pi \tag{10}$$

$$\nu_{FSR} = \nu_m - \nu_{m+1} \tag{11}$$

where m is the order of resonance, ϕ_m and $\phi_{(m+1)}$ are the phases generated from a single Bragg grating reflection at the wavelength of the m and $m+1$ order, respectively, ν_m and ν_{m+1} are the resonant frequency of the m and $m+1$ order, respectively, and L is the cavity length. Thus, by tuning the cavity phase (n or L), the resonances will drift across the stopband, and it is possible to controllably move the three resonances to the equal distant position and thus realize the phase matching condition, that is, zero FSR detuning ($FSR_1 = FSR_2$).

Here, we have integrated nickel–chromium heaters on the chip to tune the cavity phase. To avoid thermal diffusion that will heat up the grating, the heater is designed to be small compared to the cavity. A single tiny heater, however, cannot provide enough thermal tuning range because it can only

https://dx.doi.org/10.1021/acsphotonics.9b01697
ACS Photonics 2020, 7, 1009–1015

sustain limited heating powers. We experimentally designed three FPBGs whose cavity lengths have 1/3 Λ difference between each other so that the three FPBGs together can sweep across the stopband and thus realize the phase matching condition (see Supporting Information). Figure 5c shows that, by applying power on the heaters, the resonant peaks drift inside the stopband while leaving the stopband position unchanged. As shown in Figure 5d, experimentally, the FSR detuning of the central three peaks is tuned from −8.22 GHz to +0.55 GHz and is dependent on the central peak offset, namely the offset from the position of the central peak corresponding to zero FSR detuning. The larger the central peak detuning, the larger will be the FSR detuning. Although the best FSR detuning we obtained was −5.6 MHz, corresponding to the red line as shown in Figure 5c, phase matching condition is achievable with better temperature control over the integrated heater since we have successfully tuned the FSR detuning from negative to positive. By simulating the transmission spectrum of the FPBG with different cavity lengths through the transfer matrix method, we calculate the relationship of the FSR detuning and the central peak frequency detuning, and it shows good agreement with the experimental results despite some discrepancy between the experimental data of Bragg grating 1 (BG1) and the simulation results due to fabrication imperfection. This experimental result is remarkable since the simulated dispersion parameter of our current waveguide geometry is around −1400 ps/(nm km), which is in a highly normal dispersion region. It corresponds to an inherent FSR detuning of −100 MHz for a 1.39 nm FSR. We successfully compensated it by controllably leveraging the huge grating dispersion. It is worth noting that, while the FSR detuning coming from the waveguide inherent dispersion is comparable to the line width of the resonance, it will be substantial if the Q of the cavity is improved to several millions. Without the thermal tuning phase matching strategy, it would be impossible to achieve efficient wavelength conversion. Thus, such thermal tuning strategy in fact paves the way for future FPBG-FWM applications for ultrahigh-Q FPBG.

CONCLUSION

In summary, we have studied the FPBG-FWM process on a Si_3N_4/SiO_2 platform, from the theoretical framework, to the grating optimization, and the experimental realizations near 1590 nm. A −37.7 dB FWM conversion efficiency is observed with a 5.3 dBm on-chip pump power. We demonstrate that by using a tapered grating, the grating loss can be substantially reduced from 3.5 dB/cm to 0.36 dB/cm, which makes the high efficiency FWM process possible. We also demonstrate that, by thermally tuning the phase of the Fabry−Perot cavity, the phase matching condition can be realized on a relatively thin Si_3N_4 film after compensating the waveguide inherent dispersion. This phase matching technique removes the need for thick Si_3N_4 deposition, which is one of the major fabrication challenges for microring cavity based FWM process. It is worth noting that the phase matching strategy demonstrated in this work can be extended to the cases where more resonances are involved in the FPBG cavity. By adjusting the FPBG design, more resonances can exist in the stopband. Following the phase matching strategy demonstrated here, the phase matching condition can be satisfied in multiple symmetrical resonances (e.g., satisfied for resonances (−1, 0, 1), (−2, 0, 2) but not for (−2, −1, 0)) due to the nonuniform but symmetrical grating dispersion. This can be advantageous for multiplexed entangled photon pairs generation when spontaneous FWM is available since the photon pairs can only be generated on the symmetric resonances in the stopband rather than spread out until phase matching condition is no longer satisfied, as shown in multiplexed entangled photon pairs generated by ring resonator.[12,13] In the FPBG case, the power of the generated signals and the photon rates in every channel will be more uniform. Thus, such a uniform signal intensity over a given bandwidth can be preferable for applications in quantum communications. Above all, the FPBG platform is shown to be a promising approach to realize high efficiency FWM and potentially spontaneous FWM (SFWM). While the SFWM is not observable since the noise level of our OSA is higher than the SFWM level (see Supporting Information), given that the FWM efficiency is quadratically proportional to the pump power and depends on losses, we are optimistic that efficient SFWM would be achievable in future experiments with our grating approach. We envision that the FPBG-FWM will be used in many interesting applications such as controllable photon pairs generation and quantum communication.

ASSOCIATED CONTENT

Supporting Information

The Supporting Information is available free of charge at https://pubs.acs.org/doi/10.1021/acsphotonics.9b01697.

Details on four-wave mixing and spontaneous four-wave mixing efficiencies; tunability and stability of micro-heater control (PDF)

AUTHOR INFORMATION

Corresponding Author

Mario Dagenais − *Department of Electrical and Computer Engineering, University of Maryland, College Park, College Park, Maryland 20742, United States;* orcid.org/0000-0002-6758-0586; Email: dage@ece.umd.edu

Authors

Shengjie Xie − *Department of Electrical and Computer Engineering, University of Maryland, College Park, College Park, Maryland 20742, United States;* orcid.org/0000-0002-2749-2143

Yang Zhang − *Department of Electrical and Computer Engineering, University of Maryland, College Park, College Park, Maryland 20742, United States*

Yiwen Hu − *Department of Electrical and Computer Engineering, University of Maryland, College Park, College Park, Maryland 20742, United States*

Sylvain Veilleux − *Department of Astronomy, University of Maryland, College Park, College Park, Maryland 20742, United States*

Complete contact information is available at: https://pubs.acs.org/10.1021/acsphotonics.9b01697

Author Contributions

[§]These authors contributed equally.

Notes

The authors declare no competing financial interest.

https://dx.doi.org/10.1021/acsphotonics.9b01697
ACS Photonics 2020, 7, 1009−1015

■ ACKNOWLEDGMENTS

The authors acknowledge the support from NASA (Grant# 16-APRA16-0064) and National Science Foundation (Grant No. 1741651). The authors thank Jiahao Zhan, University of Maryland, for the constructive discussions. The authors would also like to acknowledge the engineering team at the Maryland Nanocenter for their help with various fabrication techniques.

■ REFERENCES

(1) Foster, M. A.; Turner, A. C.; Sharping, J. E.; Schmidt, B. S.; Lipson, M.; Gaeta, A. L. Broad-Band Optical Parametric Gain on a Silicon Photonic Chip. *Nature* **2006**, *441*, 960−963.
(2) Del'Haye, P.; Schliesser, A.; Arcizet, O.; Wilken, T.; Holzwarth, R.; Kippenberg, T. J. Optical Frequency Comb Generation from a Monolithic Microresonator. *Nature* **2007**, *450*, 1214−1217.
(3) Ferrera, M.; Razzari, L.; Duchesne, D.; Morandotti, R.; Yang, Z.; Liscidini, M.; Sipe, J. E.; Chu, S.; Little, B. E.; Moss, D. J. Low-Power Continuous-Wave Nonlinear Optics in Doped Silica Glass Integrated Waveguide Structures. *Nat. Photonics* **2008**, *2*, 737−740.
(4) Levy, J. S.; Gondarenko, A.; Foster, M. A.; Turner-Foster, A. C.; Gaeta, A. L.; Lipson, M. CMOS-Compatible Multiple-Wavelength Oscillator for on-Chip Optical Interconnects. *Nat. Photonics* **2010**, *4*, 37−40.
(5) Turner, A. C.; Foster, M. A.; Gaeta, A. L.; Lipson, M. Ultra-Low Power Parametric Frequency Conversion in a Silicon Microring Resonator. *Opt. Express* **2008**, *16*, 4881−4887.
(6) Miller, S. A.; Yu, M.; Ji, X.; Griffith, A. G.; Cardenas, J.; Gaeta, A. L.; Lipson, M. Low-Loss Silicon Platform for Broadband Mid-Infrared Photonics. *Optica* **2017**, *4*, 707−712.
(7) Ji, X.; Barbosa, F. A. S.; Roberts, S. P.; Dutt, A.; Cardenas, J.; Okawachi, Y.; Bryant, A.; Gaeta, A. L.; Lipson, M. Ultra-Low-Loss on-Chip Resonators with Sub-Milliwatt Parametric Oscillation Threshold. *Optica* **2017**, *4*, 619−624.
(8) Pu, M.; Ottaviano, L.; Semenova, E.; Yvind, K. Efficient Frequency Comb Generation in AlGaAs-on-Insulator. *Optica* **2016**, *3*, 823−826.
(9) Wang, C.; Zhang, M.; Yu, M.; Zhu, R.; Hu, H.; Loncar, M. Monolithic Lithium Niobate Photonic Circuits for Kerr Frequency Comb Generation and Modulation. *Nat. Commun.* **2019**, *10*, 978.
(10) Desiatov, B.; Shams-Ansari, A.; Zhang, M.; Wang, C.; Lončar, M. Ultra-Low-Loss Integrated Visible Photonics Using Thin-Film Lithium Niobate. *Optica* **2019**, *6*, 380−384.
(11) Zhang, M.; Buscaino, B.; Wang, C.; Shams-Ansari, A.; Reimer, C.; Zhu, R.; Kahn, J. M.; Lončar, M. Broadband Electro-Optic Frequency Comb Generation in a Lithium Niobate Microring Resonator. *Nature* **2019**, *568*, 373−377.
(12) Kues, M.; Reimer, C.; Roztocki, P.; Romero Cortés, L.; Sciara, S.; Wetzel, B.; Zhang, Y.; Cino, A.; Chu, S. T.; Little, B. E.; Moss, D. J.; Caspani, L.; Azana, J.; Morandotti, R. On-Chip Generation of High-Dimensional Entangled Quantum States and Their Coherent Control. *Nature* **2017**, *546*, 622−626.
(13) Jaramillo-Villegas, J. A.; Imany, P.; Odele, O. D.; Leaird, D. E.; Ou, Z.-Y.; Qi, M.; Weiner, A. M. Persistent Energy-Time Entanglement Covering Multiple Resonances of an on-Chip Biphoton Frequency Comb. *Optica* **2017**, *4*, 655−658.
(14) Ma, C.; Wang, X.; Anant, V.; Beyer, A. D.; Shaw, M. D.; Mookherjea, S. Silicon Photonic Entangled Photon-Pair and Heralded Single Photon Generation with CAR > 12,000 and $\hat{g}((2))(0) < 0.006$. *Opt. Express* **2017**, *25* (26), 32995−33006.
(15) Stern, B.; Ji, X.; Okawachi, Y.; Gaeta, A. L.; Lipson, M. Battery-Operated Integrated Frequency Comb Generator. *Nature* **2018**, *562* (7727), 401−405.
(16) Li, Q.; Briles, T. C.; Westly, D. A.; Drake, T. E.; Stone, J. R.; Ilic, B. R.; Diddams, S. A.; Papp, S. B.; Srinivasan, K. Stably Accessing Octave-Spanning Microresonator Frequency Combs in the Soliton Regime. *Optica* **2017**, *4* (2), 193−203.
(17) Li, Q.; Davanço, M.; Srinivasan, K. Efficient and low-noise single-photon-level frequency conversion interfaces using silicon nanophotonics. *Nat. Photonics* **2016**, *10* (6), 406−414.
(18) Kim, S.; Han, K.; Wang, C.; Jaramillo-Villegas, J. A.; Xue, X.; Bao, C.; Xuan, Y.; Leaird, D. E.; Weiner, A. M.; Qi, M. Dispersion Engineering and Frequency Comb Generation in Thin Silicon Nitride Concentric Microresonators. *Nat. Commun.* **2017**, *8* (1), 372.
(19) Braje, D.; Hollberg, L.; Diddams, S. Brillouin-Enhanced Hyperparametric Generation of an Optical Frequency Comb in a Monolithic Highly Nonlinear Fiber Cavity Pumped by a Cw Laser. *Phys. Rev. Lett.* **2009**, *102* (19), 193902.
(20) Obrzud, E.; Lecomte, S.; Herr, T. Temporal solitons in microresonators driven by optical pulses. *Nat. Photonics* **2017**, *11*, 600−607.
(21) Yu, S.-P.; Jung, H.; Briles, T. C.; Srinivasan, K.; Papp, S. B. Photonic-Crystal-Reflector Nanoresonators for Kerr-Frequency Combs. *ACS Photonics* **2019**, *6*, 2083−2089.
(22) Absil, P. P.; Hryniewicz, J. V.; Little, B. E.; Cho, P. S.; Wilson, R. A.; Joneckis, L. G.; Ho, P.-T. Wavelength Conversion in GaAs Micro-Ring Resonators. *Opt. Lett.* **2000**, *25*, 554−556.
(23) Darwish, A. M.; Ippen, E. P.; Le, H. Q.; Donnelly, J. P.; Groves, S. H. Optimization of Four-wave Mixing Conversion Efficiency in the Presence of Nonlinear Loss. *Appl. Phys. Lett.* **1996**, *69*, 737−739.
(24) Hu, Y.-W.; Zhang, Y.; Gatkine, P.; Bland-Hawthorn, J.; Veilleux, S.; Dagenais, M. Characterization of Low Loss Waveguides Using Bragg Gratings. *IEEE J. Sel. Top. Quantum Electron.* **2018**, *24*, 1−8.
(25) Lalanne, P.; Hugonin, J. P. Bloch-Wave Engineering for High-Q, Small-V Microcavities. *IEEE J. Quantum Electron.* **2003**, *39*, 1430−1438.
(26) Lalanne, P.; Mias, S.; Hugonin, J. P. Two Physical Mechanisms for Boosting the Quality Factor to Cavity Volume Ratio of Photonic Crystal Microcavities. *Opt. Express* **2004**, *12*, 458−467.
(27) Quan, Q.; Deotare, P. B.; Loncar, M. Photonic Crystal Nanobeam Cavity Strongly Coupled to the Feeding Waveguide. *Appl. Phys. Lett.* **2010**, *96*, 203102.
(28) Zhu, T.; Hu, Y.; Gatkine, P.; Veilleux, S.; Bland-Hawthorn, J.; Dagenais, M. Ultrabroadband High Coupling Efficiency Fiber-to-Waveguide Coupler Using Si3N4/SiO2waveguides on Silicon. *IEEE Photonics J.* **2016**, *8*, 1−12.
(29) Gondarenko, A.; Levy, J. S.; Lipson, M. High Confinement Micron-Scale Silicon Nitride High Q Ring Resonator. *Opt. Express* **2009**, *17*, 11366−11370.
(30) Luke, K.; Dutt, A.; Poitras, C. B.; Lipson, M. Overcoming Si_3N_4 Film Stress Limitations for High Quality Factor Ring Resonators. *Opt. Express* **2013**, *21*, 22829−22833.
(31) Pfeiffer, M. H. P.; Herkommer, C.; Liu, J.; Morais, T.; Zervas, M.; Geiselmann, M.; Kippenberg, T. J. Photonic Damascene Process for Low-Loss, High-Confinement Silicon Nitride Waveguides. *IEEE J. Sel. Top. Quantum Electron.* **2018**, *24*, 1−11.

https://dx.doi.org/10.1021/acsphotonics.9b01697
ACS Photonics 2020, 7, 1009−1015